Dissection of the Voltage Losses of an Acidic Quinone Redox Flow Battery

Qing Chen,[a] Michael R. Gerhardt, and Michael J. Aziz[*,z]

Harvard School of Engineering and Applied Sciences, Cambridge, Massachusetts 02138, USA

We measure the polarization characteristics of a quinone-bromide redox flow battery with interdigitated flow fields, using electrochemical impedance spectroscopy and voltammetry of a full cell and of a half cell against a reference electrode. We find linear polarization behavior at 50% state of charge all the way to the short-circuit current density of 2.5 A/cm^2. We uniquely identify the polarization area-specific resistance (ASR) of each electrode, the membrane ASR to ionic current, and the electronic contact ASR. We use voltage probes to deduce the electronic current density through each sheet of carbon paper in the quinone-bearing electrode. By interpreting the results using the Newman 1-D porous electrode model, we deduce the volumetric exchange current density of the porous electrode. We uniquely evaluate the power dissipation and identify a correspondence to the contributions to the electrode ASR from the faradaic, electronic, and ionic transport processes. We find that, within the electrode, more power is dissipated in the faradaic process than in the electronic and ionic conduction processes combined, despite the observed linear polarization behavior. We examine the sensitivity of the ASR to the values of the model parameters. The greatest performance improvement is anticipated from increasing the volumetric exchange current density.

Manuscript submitted October 20, 2016; revised manuscript received January 30, 2017. Published March 28, 2017.

The intermittency of wind and solar energy is motivating research on cost-effective large-scale electrical energy storage. Redox flow batteries are regarded as promising solutions as they possess many desirable attributes, including independent scaling of power and energy, long cycle life, and excellent safety.[1] The most commercially advanced RFB chemistry employs vanadium ions, whose high performance has led to MWh-scale developments. The rarity of vanadium and its variable price, however, is spurring the pursuit of alternative RFB chemistries. Among them, organic molecules such as quinones in aqueous solution are especially promising as they contain only inexpensive, earth-abundant elements and have properties that may be tuned for RFB applications. In both acidic and alkaline aqueous media, quinone-based RFBs have achieved power densities comparable to those of vanadium RFBs.[2–4]

For RFBs utilizing either vanadium ions or newer chemistries, a continuing quest is to raise the power density, as the power-conversion unit constitutes a major portion of the system cost. A broadly applicable and insightful way of evaluating factors limiting RFB power density facilitates this effort. A commonly-used method is the analysis of cell polarization – a measurement of cell potential vs. current density at fixed state of charge. The classical analysis of RFB polarization curves, inspired by fuel cell research, assigns curve slopes in different overvoltage regions to various performance-limiting factors, i.e. electrode kinetics, Ohmic resistance, and mass transport limitations (Fig. 1a).[5,6] While such polarization dissection has provided some direction to RFB design, the method has difficulty explaining the origins of polarization resistance, which is most commonly assessed after *IR*-correction based on high frequency resistance. The *IR*-correction approach convolutes membrane, electrode electronic, electrolyte ionic, and contact resistances. It offers limited insight into the difference between the DC polarization resistance and the high frequency resistance, and the role of electrolyte resistance is not apparent. Moreover, many recent works show practically linear polarization curves, even when limitations due to mass transport or faradaic reaction kinetics are shown to be significant; such findings do not support the classical dissection that assigns these two mechanisms to non-linearity.[4,7]

The classical polarization dissection does not account for the distributed nature of reaction in the porous electrode. Reaction may occur anywhere in between the ion-selective membrane and the current collector, thereby leading to different current conduction paths (Fig. 1b). The scenario of mixed ionic/electronic conductors associated with a spatially distributed faradaic reaction is described by Newman's classical porous electrode model.[8] The Newman model has been successfully applied to a variety of energy conversion/storage devices, including fuel cells and Li-ion batteries, and its basic principles can be found in many numerical models of RFBs as well.[9] Darling and Perry used it to analyze the V^{IV}/V^{V} electrode of a symmetric vanadium RFB with a variety of flow fields.[7] They deduced the DC electrode resistance from the measured resistances of the cell, the membrane, and the contacts, and used the solution of the 1-D porous electrode model to assign a value of the volumetric exchange current density (the product of the exchange current density i_0 and specific surface

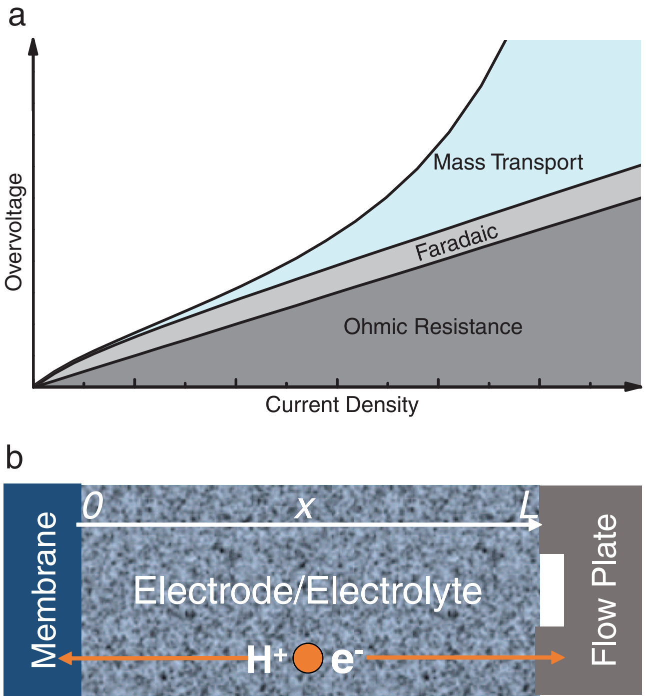

Figure 1. (a) Classical dissection of a RFB polarization curve (topmost curve) into overvoltages from Ohmic, faradaic, and mass transport processes. (b) Sketch of a reacting porous electrode in a RFB (a half of the cell is shown as the other half mirrors it across the membrane).

---

[a] Present address: Department of Mechanical and Aerospace Engineering, Hong Kong University of Science and Technology, Kowloon, Hong Kong.
[*] Electrochemical Society Member.
[z] E-mail: maziz@Harvard.edu

area, or area per unit volume, *a*) and to evaluate a value of the resistance of the faradaic reaction in the regime of linear kinetics.

Recently, Sun et al.[10] performed electrochemical impedance spectroscopy (EIS) on symmetric V^{II}-V^{III} cells and modeled the results over frequencies down to 1 mHz in order to separately identify overvoltages from mass transport limitations, faradaic charge transfer, and Ohmic processes. Because the V^{II}-V^{III} kinetics are sluggish and the cells were operated at low flow rates, they found that losses due to Ohmic processes were dwarfed by those due to mass transport processes which, in turn, were dwarfed by those due to faradaic processes. Thus no effort was devoted to distinguishing among the Ohmic processes. Our research on organic redox systems with much faster faradaic kinetics[2,3] leads us to a study of overvoltages in a regime in which Ohmic processes and faradaic processes provide roughly equal losses. Thus we have developed a dissection approach that permits us to separately evaluate the Ohmic losses from electrode electronic, contact electronic, electrolyte ionic, and membrane ionic processes and to consider them alongside the losses in the faradaic process. In the present work, we restrict our attention to electrolyte flow rates high enough that mass transport overvoltages may be neglected. Our work also provides an explicit experimental evaluation of the decay length of the faradaic reaction with distance from the membrane, which we use to obtain a value of the volumetric exchange current density by fitting to the Newman model, obtaining good agreement with the value we obtain by using the method of Darling and Perry. This work provides direct guidance for cell engineering for enhanced performance.

We first employ half-cell and voltage-probe experiments to evaluate the polarization resistance and the reaction distribution within the electrode, in a quinone-bromide flow battery (QBFB). We perform these measurements at 50% state of charge (SOC) and high flow rate so that reactant mass transport limitations are negligible. We then interpret the results within the context of the 1-D Newman model to reveal the various contributions to the resistance in a linear polarization curve and its connection to the reaction distribution. We find that, for sufficiently thin electrodes, despite the lower conductivity of the ionic pathway the fraction of current in the electrode carried by the electrolyte varies linearly across the thickness, indicating a spatially homogeneous reaction; for electrodes that are "too thick", the fraction approaches that in two parallel resistors, heavily weighted toward the higher-conductivity solid phase. Our results and interpretation provide an approach to the detailed analysis of linear polarization curves.

Experimental

Full-cell measurements.—The cell design follows that of Ref. 4. On each side, a commercial graphite plate with interdigitated flow channels (Fuel Cell Tech, Albuquerque, NM) was used to feed electrolyte to a porous carbon paper electrode at a rate of 100 mL/minute controlled by a MasterFlex (Cole Parmer) diaphragm pump. It has been shown that raising the flow rate by a factor of four makes a negligible difference in the polarization curves.[4] The temperature of the cell was approximately 20°C. The electrode comprised a stack of 3 sheets of SGL 10AA (each nominally 400 μm thick) carbon paper, compressed to ~75% of the original thickness, defined by Teflon gaskets. The geometric area of the electrodes was 2 cm^2. The SGL paper was pre-treated by baking at 400°C in air for 24 hours. A Nafion 212 membrane served as the ion-selective membrane. Its pre-treatment consisted of heating in DI water at 85°C for 15 min., followed by soaking in 5% hydrogen peroxide for 30 min., and then by soaking in 0.05 M H_2SO_4 for 1 hour. As assembled, the negative electrolyte ("negolyte") (20 mL) contained 1 M 9,10-anthraquinone-2,7-disulfonic acid (AQDS), ion exchanged from its sodium salt (TCI), and 1 M H_2SO_4, and the positive electrolyte ("posolyte") (24 mL) contained 3 M hydrobromic acid and 0.5 M Br_2. The nominal reactions during the charging process on the negative and positive sides, respectively, are as follows:

$$\mathrm{AQDS} + 2\mathrm{H}^+ + 2\mathrm{e}^- \rightarrow \mathrm{H_2AQDS};$$

$$2\mathrm{Br}^- - 2\mathrm{e}^- \rightarrow \mathrm{Br}_2.$$

They are reversed during discharging. Because the negative side is the capacity-limiting side, we define the cell SOC as the state of charge of the negolyte, i.e. the instantaneous ratio of nominal hydroquinone concentration (assuming no reactions other than the pair listed above) to the total nominal quinone + hydroquinone concentration.

Electrochemical tests were carried out by a Gamry 30k booster connected to a Gamry Reference 3000 potentiostat. Polarization curves were recorded by measuring the current during linear sweeping at a rate of 100 mV/s. We find that this method yields the same relationship between voltage and current density as do potentiostatic or galvanostatic holding tests in our experimental setup, but without significantly changing the SOC of the relatively small volume of electrolytes used in the tests. Polarization curves at 50% SOC are discussed here, as they well represent the cell polarization behavior. To reach this SOC, a charge threshold, derived from the charge capacity measured in the first cycle, was set during a potentiostatic charging process at 1.3 V. High frequency area-specific resistance (ASR) values, r^{HF}, were evaluated from EIS at ~100 kHz. The electrode electronic ASR and the contact resistance were evaluated by direct DC measurements in a dry cell, which consisted of the same flow cell except without electrolytes and membrane.

Half-cell measurements.—The cell was set up similarly to that in the full-cell test, except that a palladium-hydrogen (Pd-H) reference electrode was sandwiched between two Nafion 115 membranes, which were soaked in DI-water at room temperature for ~24 hours prior to the experiments. The Pd-H electrode was prepared according to Ref. 11. The reference electrode was prepared from a 125 μm thick Pd foil. It has a potential of ~50 mV vs. reversible hydrogen electrode. A potential change of less than 5 mV was usually measured prior to and right after the half-cell experiments, indicating that the reference electrode potential is stable to within about 5 mV. The Pd-H electrode was placed against the membranes, immediately above the upper edge of the porous electrodes (Fig. 2a).[12]

Potential-probe experiments.—25 μm thick gold foil was cut into 0.5 mm wide strips, and sandwiched between sheets of porous electrode as shown in Fig. 2a, in a manner similar to the placement of Pt probes in Ref. 13. The inclusion of the probes did not affect the cell characteristics in either full-cell polarization or dry-cell measurements. During cell polarization, voltage differences between adjacent probes were recorded by voltmeters of high impedance (>10^{14} Ω).

Results

Full-cell polarization.—The solid line in Fig. 2b is the polarization curve for the QBFB at 50% SOC. The small oscillations are caused by the pulsation of the diaphragm pump. The curve is nearly linear and its average slope provides an evaluation of the total polarization ASR, r^{DC}_{full} = 326 mΩcm^2. This comprises contributions from the negative and the positive electrodes (r^{DC}_{neg} and r^{DC}_{pos}, respectively), a membrane ASR (r_{N212}), and the area-specific contact resistance (r_C) of each side:

$$r^{DC}_{full} = r^{DC}_{pos} + r^{DC}_{neg} + r_{\mathrm{N212}} + 2r_C, \qquad [1]$$

where we have assumed r_C to be the same on both sides. The electrode contributions include all the remaining factors that contribute to cell polarization, which will be discussed in the next section.

The membrane and contact resistances are expected to be Ohmic. They can be evaluated by combining high-frequency EIS and dry-cell measurements. At high frequencies, where the faradaic reactions are frozen out and replaced by capacitive coupling across the electrode/electrolyte interface, EIS gives an ASR of r^{HF}_{full} = 101 mΩcm^2.

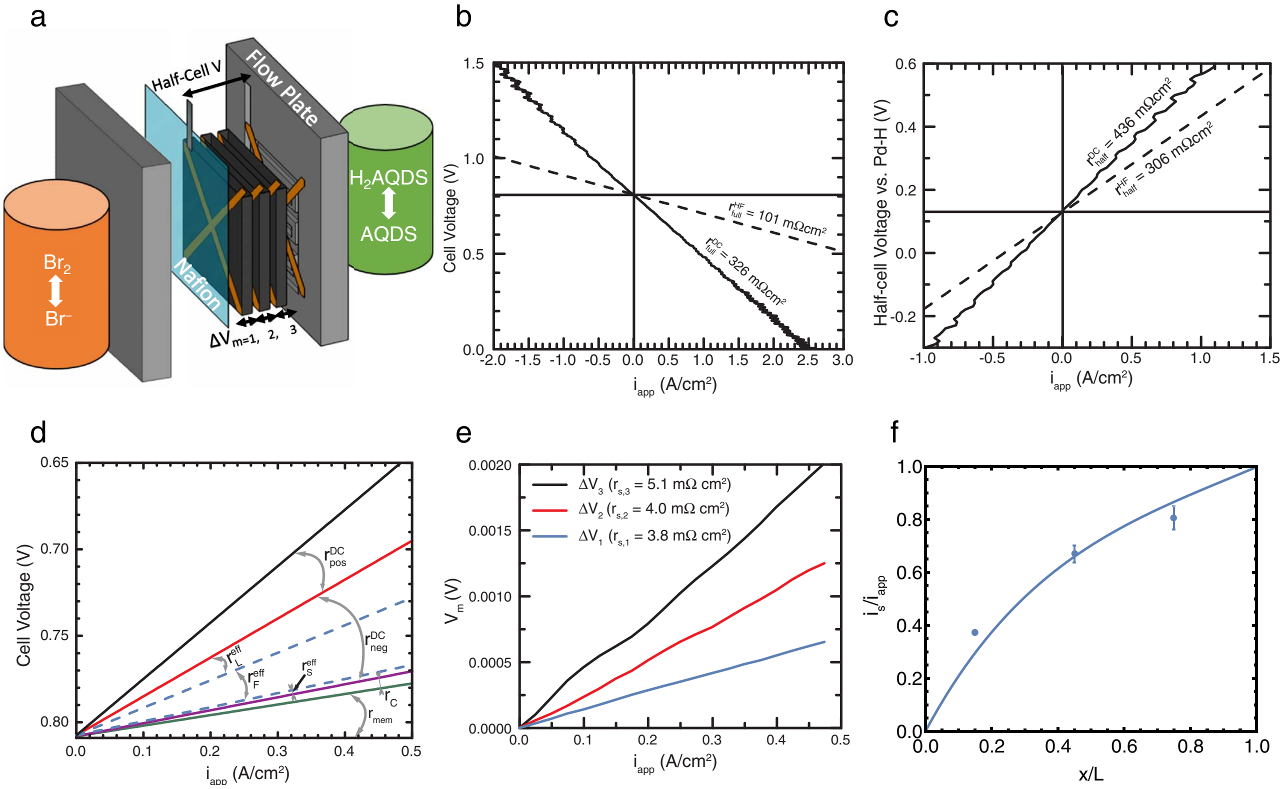

Figure 2. (a) Illustration of half-cell and voltage-probe experiments. (b) Full-cell and (c) negative half-cell polarization curves (solid lines) vs. macroscopic applied current density at 50% SOC; the dashed lines correspond to overvoltage contributions estimated by $r^{\mathrm{HF}} \times i_{app}$. Wiggles in the measured curves come from the pump pulsation. (d) Dissection of the full-cell polarization curve (topmost curve) into contributions from the negative and the positive electrode, the contact resistances, and the membrane ASR (solid lines), and further dissection of r^{DC}_{neg} into effective resistances due to faradaic, ionic conduction and electronic conduction processes distributed within the electrode (dashed lines). (e) Voltage-probe signals recorded between the probes shown in (a), during a polarization measurement at 50% SOC; dry-cell electronic ASR values are reported for comparison, showing much less variation than the slopes of the curves. (f) Circles: electronic current vs. distance from membrane as deduced from the voltage-probe measurement at 0.2 A/cm^2 and dry-cell layer ASR values; error bars come from repeated measurements in the same cell. Solid curve comes from the Newman model, Eq. 15, with parameters in Table I and the volumetric exchange current density of the faradaic reaction given by $ai_0 = 2.45$ A/cm^3.

This comprises the ionic ASR from the membrane and the ASR from the electrode (r^{HF}_e) and the contact on each side as follows:

$$r^{HF}_{full} = 2r^{HF}_e + r_{\mathrm{N212}} + 2r_C, \qquad [2]$$

assuming r^{HF}_e to be the same on both sides and r_C to be the same on both sides[b]. r^{HF}_e is the high-frequency resistance of the porous electrode filled with the electrolyte, given by

$$r^{HF}_e = \frac{r_S r_L}{r_S + r_L}, \qquad [3]$$

where r_S is the electronic ASR of the electrode, and r_L is the ionic ASR of the electrolyte;[14] they are in parallel in this mixed electron-ion conductor. r_L can be estimated from the bulk electrolyte resistance based on the Bruggeman correction (electrolyte conductivity $\kappa = \kappa_0\epsilon^{1.5}$, where ϵ is the porosity) to be 308 mΩcm^2. We measured the values of r_S and r_C in a dry cell. We estimate r_C by extrapolating a plot of dry-cell ASR vs. electrode thickness, which is varied by varying the number of stacked sheets of identical carbon paper, compressed by the same percentage of the original thickness, to zero electrode thickness. We thereby obtain $r_S = 13.2$ mΩcm^2 and $r_C = 6.8$ mΩcm^2 for each side. r^{HF}_e is therefore 12.7 mΩcm^2. From Eq. 2, we obtain an estimate of $r_{\mathrm{N212}} = 62.1$ mΩcm.[2] This value for the membrane ASR agrees with other measurements of Nafion 212 taken in similar acidic electrolytes.[15]

Half-cell polarization.—The polarization of the negative or the positive side can be separately investigated by installing a reference electrode in the QBFB. Here we focus our study on the negative, quinone-bearing side, in order to determine r^{DC}_{neg} for use in the full-cell analysis described above. A palladium-hydrogen (Pd-H) reference electrode was sandwiched between two Nafion 115 membranes. The hydrogen in the Pd-H and the protons in the membranes equilibrate at a stable voltage of ∼50 mV vs. reversible hydrogen electrode. The voltage of the current collector of the negative half-cell is recorded against the Pd-H electrode during the half-cell polarization. The curve at 50% SOC (Fig. 2c) shows an ASR of $r^{DC}_{half} = 436$ mΩcm^2; this is higher than r^{DC}_{full} of the full cell due to the use of a thicker membrane in the half-cell polarization experiments. The expressions analogous to Eqs. 1 and 2 for the half-cell measurement are

$$r^{DC}_{half} = r^{DC}_{neg} + r_{\mathrm{N115}} + r_C; \qquad [4]$$

$$r^{HF}_{half} = r^{HF}_e + r_{\mathrm{N115}} + r_C. \qquad [5]$$

After subtracting the membrane resistance ($r_{N115} = 286$ mΩcm^2, deduced through an approach similar to that described in the previous paragraph) and r_C off of r^{DC}_{half}, we find that $r^{DC}_{neg} = 143$ mΩcm^2. Substituting this value of r^{DC}_{neg} into Eq. 1 permits us to deduce that the value of r^{DC}_{pos} is 107 mΩcm^2. This dissection is plotted as solid lines in Fig. 2d.

Voltage-probe measurements.—To understand the reaction distribution and its influence on electrode polarization, we quantified the current distribution in the electrode through the use of voltage probes.

---

[b] We make no distinction between the DC and high-frequency AC ASRs of purely Ohmic elements such as the membrane, the contacts, the solid phase of the electrode, and the liquid electrolyte.

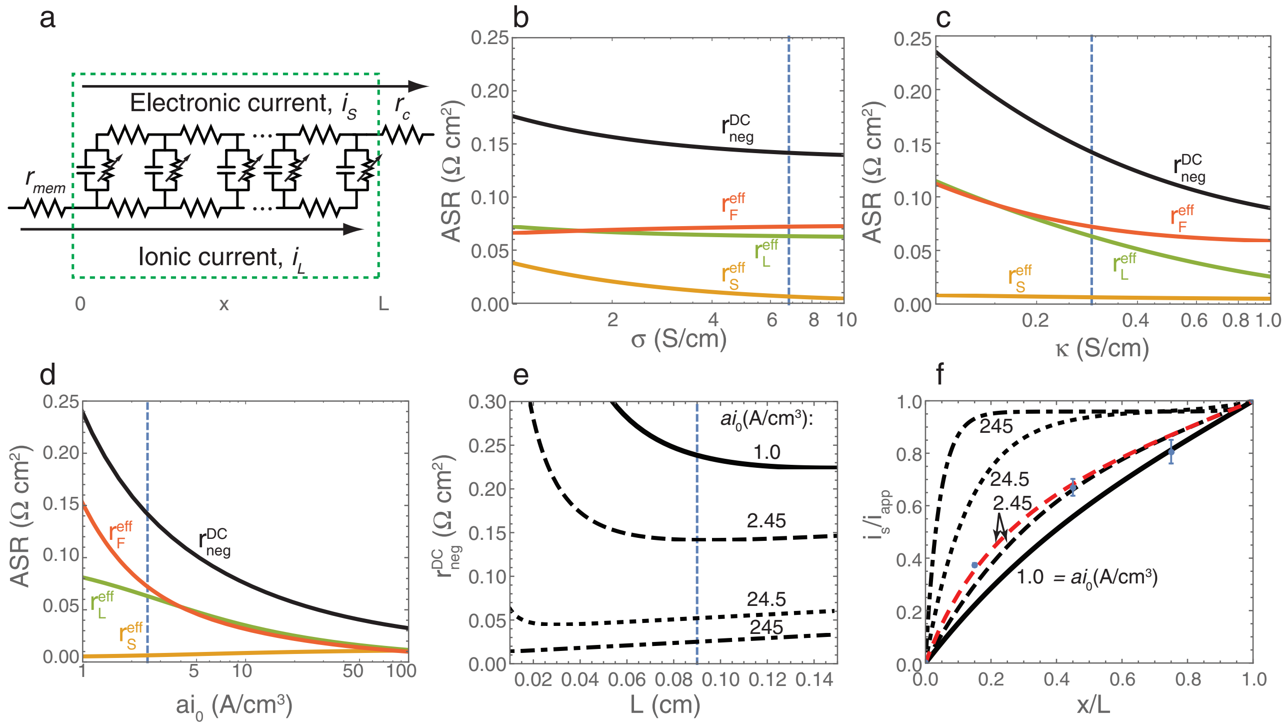

Figure 3. (a) An equivalent circuit representing the half-cell in the infinitesimal limit. The circuit for the electrode is bounded by the dashed rectangle. (b)-(f) Parameter sensitivity. The negative electrode polarization ASR (black) and the effective ASR contributions vs. (b) the electrode electronic conductivity, (c) the electrolyte ionic conductivity, and (d) the volumetric exchange current density of the faradaic reaction. Note that the colored lines in (b)-(d) represent both the power dissipated in each effective ASR contribution and the partial derivatives of r^{DC}_{neg} defined in Equations 22–24. (e) r^{DC}_{neg} vs. electrode thickness with various values of ai_0, and (f) fraction of applied current that is electronic vs. distance from the membrane for these values of ai_0. The red dashed line in (f) represents the current distribution at 0.5 A/cm^2 under the assumption of Tafel kinetics with $ai_0 = 2.45$ A/cm^3; the black lines all represent linear kinetics. The vertical dashed lines in (b)-(e) and the blue circles in (f) represent the experimental cell. Unspecified parameters are taken from Table I.

Voltage drops across each layer of carbon paper (ΔV_m, $m = 1$, 2 or 3) were recorded by gold probes, as plotted in Fig. 2e vs. the applied current density i_{app}. The electronic ASR through each layer of carbon paper ($r_{S,m}$) was also measured via the probes in a dry-cell. The values are listed in Fig. 2e, and their sum, 12.9 mΩcm^2, is approximately equal to the value of r_S reported above. Dividing each value of ΔV_m by the corresponding value of $r_{S,m}$ gives us the average electronic current density, $i_{S,m}$, traversing each sheet during the wet-cell polarization experiments. In Fig. 2f we assign this sheet-average value of $i_{S,m}$ to the center position of each sheet ($x = (m\text{-}1)L/3 + L/6$, where L is the electrode thickness after compression) in order to guide our visualization of the current distribution (the points in Fig. 2f). The values determined for i_S/i_{app} are reasonably independent of i_{app}, as a result of the linearity of the curves in Fig. 2e; the small oscillations are due to the diaphragm pump. This is consistent with the linearity of the polarization curves.

Discussion

In this section, we use the Newman porous electrode model to calculate the ionic and electronic current distributions and the electrode resistance in the polarization of the QBFB and to interpret the experimental results. We also use the model to derive separate contributions to power dissipation from the faradaic, electrode electronic, and electrolyte ionic processes within the electrode, and to offer an interpretation in terms of effective contributions to the polarization resistance from these respective processes.

We start with a brief recapitulation of the model. It considers a one-dimensional (1-D) porous interpenetrating electrode/electrolyte continuum wherein properties vary smoothly along the thickness direction ($0 \le x \le L$, as shown in Fig. 1b). The electrical currents in the liquid (electrolyte) and the solid (electrode) phases obey Ohm's law, and the current transferred between the phases in the faradaic reaction is a function of the local potential difference between the two phases. The equivalent DC circuit is the infinitesimal limit of the transmission line depicted in Fig. 3a. If we define the potentials in the solid and the liquid phases as φ_S and φ_L, and the current densities as i_S and i_L, respectively, the governing equations in the model are as follows

$$i_S = -\sigma\frac{d\varphi_S}{dx}, \qquad [6]$$

$$i_L = -\kappa\frac{d\varphi_L}{dx}, \qquad [7]$$

$$\frac{di_{app}}{dx} = 0, \qquad [8]$$

$$i_S + i_L = i_{app}, \qquad [9]$$

where σ is the electronic conductivity of the porous electrode and κ is the ionic conductivity of the pore-filling electrolyte. Note that all conductivities discussed in this work are effective macroscopic values that include effects from electrode porosity: the value of σ is smaller than the conductivity of bulk solid, non-porous electrode material due to the porosity; the value of κ is smaller than the conductivity of bulk electrolyte due to the geometry of the electrolyte-filled pores. From continuity and solution charge neutrality, the divergence of the liquid phase current density is equal to the local faradaic current density. The Butler-Volmer equation governing the faradaic current can then be written as

$$\frac{di_L}{dx} = -\frac{di_S}{dx} = ai_0\left(e^{-\frac{\alpha nF}{k_BT}(\varphi_S-\varphi_L-U)} - e^{\frac{(1-\alpha)nF}{k_BT}(\varphi_S-\varphi_L-U)}\right), \qquad [10]$$

where α is the charge transfer coefficient, n is the electron transfer number, k_B is the Boltzmann constant, F is Faraday's constant, and T is the absolute temperature. U is the open-circuit value of $\varphi_S - \varphi_L$ and is taken as zero here, as φ_L can be assessed with the same reference electrode as the electrode of interest. Boundary conditions in the model are

$$\text{At } x = 0\text{: } i_L = i_{app},\ \varphi_L = 0;$$

$$\text{At } x = L\text{: } i_S = i_{app}.$$

The model can be visualized by an equivalent circuit shown in Fig. 3a, i.e. the transmission line model. The faradaic components in the circuit connect the electronic and the ionic resistors, which terminate at the membrane and the current collector, respectively, and operate in series for any particular trajectory through the electrode.

We use the model to apportion the power dissipation within the electrode among the three components – electronic, ionic and faradaic. The power dissipated, per unit of macroscopically-measured geometric area, by the solid electronic, the liquid ionic, and the faradaic process, respectively, is

$$p_S = \int_0^L \frac{(i_S(x))^2}{\sigma} dx; \qquad [11]$$

$$p_L = \int_0^L \frac{(i_L(x))^2}{\kappa} dx; \qquad [12]$$

$$p_F = \int_0^L \frac{di_S(x)}{dx}(\varphi_S(x) - \varphi_L(x))dx. \qquad [13]$$

These expressions are not restricted to linear faradaic kinetics; also they may be generalized to deal with three-dimensional current distributions. They provide the basis for our later discussion of the contributions of each mechanism to the polarization resistance.

We proceed with following assumptions:

- Because the active species in RFBs possess rapid kinetics (i.e. $ai_0 \geq i_{app}/L$, according to the criterion of Newman et al.[16]), the arguments of the exponentials in Eq. 10 are small and the equation can be linearized as

$$\frac{di_L}{dx} = ai_0 \frac{nF}{k_B T}(\varphi_S - \varphi_L). \qquad [14]$$

- κ is assumed independent of x. This is a valid approximation when the main charge carrying ion has a sufficiently high concentration and/or diffuses sufficiently rapidly that perturbations to the ionic strength due to the faradaic reaction are negligible; this is the case in all-vanadium RFBs as well as the QBFB.
- Mass transport does not limit cell polarization so that concentrations of the active species remain the same as their starting values throughout the electrode. This assumption is reasonable at high flow rate in the QBFB based on experimental observations[4] of an insignificant dependence of ASR on flow rates of $Q \geq 100$ mL/min. The stoichiometric flow rate is given by $nC_{H_2AQDS}Q$, where C_{H_2AQDS} is the reactant concentration. At $Q = 100$ mL/min and 50% SOC, $nFC_{H_2AQDS}Q/A = 32$ A/cm^2 (where A is the geometric electrode area), which is more than an order of magnitude greater than the highest value of i_{app} examined in this study.

These assumptions allow for analytical solutions to the current distributions. The normalized electronic current i_S/i_{app} is thus the following function of x:

$$\frac{i_S}{i_{app}} = \frac{\kappa}{\kappa + \sigma}\left[1 + \frac{(\sigma/\kappa)\sinh(\nu - \nu x/L) - \sinh(\nu x/L)}{\sinh \nu}\right], \qquad [15]$$

where

$$\nu \equiv \sqrt{\frac{Fai_0L^2}{RT}\left(\frac{1}{\kappa} + \frac{1}{\sigma}\right)}. \qquad [16]$$

Due to the linearization of the Butler-Volmer equation, the nonlinear faradaic impedances between the electronic and the ionic resistors of Fig. 3a are replaced by Ohmic resistors, leading to a current density-independent electrode ASR of

$$r_{neg}^{DC} = \frac{L}{\sigma + \kappa}\left[1 + \frac{2 + (\frac{\sigma}{\kappa} + \frac{\kappa}{\sigma})\cosh \nu}{\nu \sinh \nu}\right]. \qquad [17]$$

The linearized Bulter-Volmer also allows us to apportion r_{neg}^{DC} into effective contributions from electronic, ionic and faradaic resistances based on their power dissipations (Eqs. 11–13). We can divide the power losses by $i_{app}{}^2$, which yields values for their effective ASRs as

$$r_S^{eff} \equiv \frac{p_S}{i_{app}^2} = \frac{1}{\sigma}\int_0^L \left(\frac{i_s(x)}{i_{app}}\right)^2 dx; \qquad [18]$$

$$r_L^{eff} \equiv \frac{p_L}{i_{app}^2} = \frac{1}{\kappa}\int_0^L \left(1 - \frac{i_S(x)}{i_{app}}\right)^2 dx; \qquad [19]$$

$$r_F^{eff} \equiv \frac{p_F}{i_{app}^2} = \int_0^L \frac{di_S(x)}{i_{app}{}^2 dx}(\varphi_S(x) - \varphi_L(x))dx; \qquad [20]$$

$$= \frac{k_B T}{ai_0 nF}\int_0^L \left(\frac{d(i_S(x)/i_{app})}{dx}\right)^2 dx. \qquad [21]$$

The three effective ASRs are thus functions of the current distribution, which is the solution to Eq. 15.

All parameters of the QBFB needed in Eqs. 10–21 can be quantified to a fair degree of accuracy (Table I), except the specific surface area a and the exchange current density i_0. Therefore we combine them into a single fitting parameter ai_0, which we have called the volumetric exchange current density of the faradaic reaction; this can be evaluated by solving Eq. 17 for ν, where the left hand side comes from half-cell polarization (Fig. 2c). With $r_{neg}^{DC} = 143$ mΩcm^2, ai_0 in the negative side of the QBFB is calculated to be 2.45 A/cm^3 from Eqs. 16–17. The ai_0 value can also be estimated by fitting the measured current distribution to that calculated from Eq. 15, which is 2.65 A/cm^3. The agreement between the two ai_0 estimates confirms the applicability of the Newman model to the case studied here. Using Eqs. 18–21 with $ai_0 = 2.45$ A/cm^3, we evaluate r_S^{eff}, r_L^{eff}, and r_F^{eff} to be 6.3, 64, and 73 mΩcm^2, respectively (dashed lines in Fig. 2d). Therefore, the electrode suffers more power dissipation from faradaic processes than

Table I. Cell parameters in the QBFB. Note that: (1) the reported electrode thickness and conductivity account for compression; (2) the electrolyte conductivity is calculated based on the measured bulk conductivity and is corrected with the Bruggeman correction ($\kappa = \kappa_0 \epsilon^{1.5}$); (3) the measurement process of the electrode electronic conductivity can be found near the start of the Results section. Here, to simplify the calculation, we assume the electron conductivity to be independent of position despite the differences among the measured values of $r_{S,m}$ (Fig. 2e). Calculated results, in turn, indicate that the difference among the values of $r_{S,m}$ is too small to significantly affect the reaction distribution and the value of r_{neg}^{DC}.

Electrode Thickness, L (cm)	0.09	Electrolyte Conductivity (corrected), κ (S/cm)	0.292
Electrode Conductivity, σ (S/cm)	6.82	Electron Transfer Number, n	2
Charge Transfer Coefficient, α	0.5	Temperature, T (K)	293

from electronic and ionic resistance combined, despite the linearity of the polarization curve.

We now interpret the electrode polarization resistance with insights from the Newman model. r_{neg}^{DC} includes contributions from electrode electronic, electrolyte ionic and faradaic charge transfer resistances, and mass transport. We neglect mass transport limitations, as is assumed in the model. The remaining three contributors enter the model through the kinetic parameters σ, κ, and ai_0, respectively. They combine to determine the current distribution in the electrode, and thereby determine the electrode polarization resistance.

Within the context of the model, the effective ASRs r_S^{eff}, r_L^{eff}, and r_F^{eff}, defined in Eqs. 18–21, respectively, from considerations of power dissipation, also turn out to satisfy

$$r_S^{eff} = \frac{\partial r_{neg}^{DC}(\sigma, \kappa, ai_0)}{\partial \ln(1/\sigma)}; \qquad [22]$$

$$r_L^{eff} = \frac{\partial r_{neg}^{DC}(\sigma, \kappa, ai_0)}{\partial \ln(1/\kappa)}; \qquad [23]$$

$$r_F^{eff} = \frac{\partial r_{neg}^{DC}(\sigma, \kappa, ai_0)}{\partial \ln(1/ai_0)}. \qquad [24]$$

Thus they may be interpreted as the sensitivity of the ASR to the relevant kinetic parameters.[c]

We show the sensitivity of r_{neg}^{DC} to changes in the kinetic parameters in Figs. 3b, 3c, and 3d. Because σ here is an order of magnitude greater than κ, a change in the value of σ brings little change to the polarization resistance, whereas r_{neg}^{DC} is more sensitive to κ. We note that r_F^{eff} changes with κ as well, due to the variation in the current distribution accompanying a variation in κ.

Unlike σ and κ, which can be varied only within a narrow range, the value of ai_0 may be expected to vary by orders of magnitude, and thereby exert the most significant influence on the value of r_{neg}^{DC} (Fig. 3d). Fig. 3f shows the corresponding current distributions at a variety of values of ai_0. At all values except the lowest, the reaction zone (the part of the curve with steep slope) is near the membrane because the much higher value of σ drives the centroid of the reaction toward the membrane so as to minimize the unfavorably resistive ionic conduction path. As the range of ai_0 spanned in Fig. 3d is traversed, most of the dissipation is contributed by the electrolyte and the faradaic reaction, until the value of ai_0 becomes large enough that the thick electrode only adds electronic resistance. At low ai_0, the effective faradaic ASR dominates r_{neg}^{DC}. The dependence of all three effective ASRs on ai_0 also reminds us that they do not actually exist in isolation from each other, as the current distribution in the solution to the model equations originates from the interplay among all parameters.

With high values of ai_0, a plateau appears in the depth distribution of the electronic current (Fig. 3f) at the value $\sigma/(\sigma + \kappa)$, apportioning the current to the electrode and electrolyte phases as in a circuit involving two resistors in parallel, connected only at their ends. No faradaic reaction occurs within the plateau – a strong indication that the electrode is too thick to be practical. In a plot of r_{neg}^{DC} vs. the electrode thickness (Fig. 3e), there exists an optimal thickness, below which the low surface area adds faradaic resistance, and above which the increasing electronic resistance outweighs the benefit of additional surface area. The existence of such an optimal electrode thickness is in line with experimental observations.[7,17]

This discussion is based on the linearized Butler-Volmer assumption, which is applicable when the applied current density i_{app} is below[8] $ai_0L = 0.21$ A/cm^2. When i_{app} exceeds this limit, as it did in our experiments, we would expect the differential electrode polarization resistance to decrease, becoming dependent on i_{app}. Our experimental observation, however, shows r_{neg}^{DC} remains practically constant up to 0.5 A/cm^2. A possible explanation is that the change in r_{neg}^{DC} with i_{app} is too small to appear in these measurements. In the current density range of 0.21–0.5 A/cm^2, neither linearized Butler-Volmer nor Tafel kinetics yields an accurate solution in the Newman model. But as we compare side by side (Fig. 3f) the current distributions at 0.5 A/cm^2 predicted based on the Tafel and the linear Butler-Volmer kinetics (the latter of which is independent of i_{app}, and thus is the same as at 0.2 A/cm^2), their difference is indeed small. This supports our explanation of the apparently constant value of r_{neg}^{DC} in the current density range examined in Fig. 2d. We do not believe the difference in proximity to the experimental point at $x/L = 0.15$ in Fig. 2f to be particularly significant, given that we discretized the electronic current distribution in the analysis of the experiment, assumed layer-independent electronic conductivities despite the layer-dependence revealed by the voltage probes, and assumed zero contact resistance between the sheets of carbon paper.

The low fitted value of ai_0, 2.45 A/cm^3, also merits attention. If we were to assume that $a = 200$ cm^2/cm^3 (measured with Toray carbon paper,[18] and thus could be an underestimate for SGL 10AA), and $k = 7.2 \times 10^{-3}$ cm/s (measured on glassy carbon at an AQDS concentration of 1 mM),[3] the value of ai_0 at 50% SOC, given by

$$ai_0 = ankF(C_{AQDS}C_{H_2AQDS})^{0.5}, \qquad [25]$$

would be 70 A/cm^3, which is more than an order of magnitude higher than the fitted value. There are many possible explanations for such a discrepancy, including imperfect wetting of the electrode, the inaccuracy of extrapolating dilute solution kinetics to that of concentrated electrolytes, and mass transport limitations.

Because the processes in the QBFB are common among other RFB systems, we believe that the approach taken here can be widely applicable. It provides a framework that embraces the reaction distribution within the porous electrode and the interplay between electrolyte, electrode, and the reaction at their interface, and thus enables the interpretation of linear polarization curves. We note that the voltage-probe measurements serve essentially to verify the applicability of the Newman model to our experiments while independently establishing the value of ai_0. Thus, with enough confidence in the applicability of the 1-D model to the electrodes of an operating cell, one can use the method of Darling and Perry[7] to infer the faradaic resistance from measured cell polarization resistance and membrane and contact resistance. This, or any other method of establishing values for ai_0 and membrane and contact resistances, provide sufficient information to uniquely identify the power dissipation in the electrolyte, in the electrode solid phase, and in the faradaic process, as well as in the membrane and in the electron-conducting contacts, thereby providing insight into factors limiting RFB performance.

We end this discussion by pointing out the limitations of this simple model. It neglects the potential for mass transport limitation, in which the consumption rate of reactant at the surface of the porous electrode is high enough to cause a significant decrease in the local reactant concentration. This may be manifested in the form of an increased apparent value of r_{neg}^{DC} at high current densities, leading to an underestimate of ai_0. The linearity of the polarization curves suggests that this effect is insignificant over the range of current densities examined in this work, which is consistent with our neglect of the phenomenon in this study. It is possible, however, that the effect is offset quantitatively by that of nonlinear faradaic reaction kinetics. The experimental observation of a weak, but nonzero, variation of ASR with flow rate at $Q = 100$ mL/min indicates a subtle effect of mass transport not captured by this model. At lower stoichiometric flow rates and higher current densities, mass transport effects will be essential for a reliable model. Additionally, in the 1-D model, no in-plane distribution of reaction and conduction is considered. It is reasonable to expect 2-D and 3-D models to exhibit effects such as a distribution of electron conduction paths, with electrons generated over the channel traveling significant distances laterally. Accounting for transport effects such as these is an important topic for future research.

---

[c] Note that an analogous interpretation also holds for two simple resistors in series, or for a simple resistor in series with two resistors in parallel.

Conclusions

We have dissected the polarization resistance of the QBFB via half-cell and voltage-probe measurements. The full cell total polarization ASR, i.e. $r_{full}^{DC} = 326$ mΩcm^2, is dominated by the electrode polarization resistances, 143 mΩcm^2 of which comes from the negative electrode and 107 mΩcm^2 of which comes from the positive electrode. The balance comes from membrane ionic resistance (62 mΩcm^2) and electronic contact resistance (14 mΩcm^2). The experimentally measured cell ASR and voltage distribution in the negative electrode are consistent with a calculation of the electronic current distribution based on the Newman 1-D porous electrode model.

Fitting the model to experiment yields a value of the volumetric exchange current density of $ai_0 = 2.45$ A/cm^2, and permits us to further dissect the ASR of the negative electrode by quantifying the power dissipation in the interfacial faradaic, electrode electronic, and electrolyte ionic transport processes. In Eqs. 18–20 we define the effective ASR for each of these three processes as the ratio of power dissipation to the square of the applied current density, resulting in values for the negative electrode of $r_F^{eff} = 73$ mΩcm^{22} $r_S^{eff} = 6.3$ mΩcm^2, and $r_L^{eff} = 64$ mΩcm^2. Thus we find that, in the negative electrode of the cell studied here, more power is dissipated in the faradaic process than in the electronic and ionic transport processes combined.

Eqs. 22–24 indicate a correspondence between the effective ASRs of these three processes and the sensitivity of the electrode polarization ASR to the values of the corresponding kinetic parameters. The model predicts that the electrode thickness is near optimal for the present values of the kinetic parameters but that a boost in ai_0, accompanied by a decreased electrode thickness, may significantly lower the polarization ASR.

Acknowledgments

This work was funded partially through the US Department of Energy ARPA-E Award DE-AR0000348 and partially through the Harvard John A. Paulson School of Engineering and Applied Sciences. This work was also supported by funding from the Massachusetts Clean Energy Technology Center. We thank Marc-Antoni Goulet, David Kwabi, Andrew Wong, Professor Na Li, and Professor Allen J. Bard for helpful discussions.

List of Symbols

a	Specific surface area, cm^2/cm^3
C	Reactant concentration, mol/L
F	Faraday's constant, C/mol
i	Current density, A/cm^2
i_0	Exchange current density, A/cm^2
k	Electrochemical rate constant, cm/s
k_B	Boltzmann's constant
L	Electrode thickness, cm
n	Number of transferred electrons
p	Power dissipated per unit area, W/cm^2
Q	Flow rate, mL/min
r	Area specific resistance, Ω cm^2
T	Temperature, K
U	Open-circuit value of $\phi_S - \phi_L$

Greek

α	Charge transfer coefficient
ϵ	Porosity
κ	Electrolyte conductivity, S/cm
σ	Electronic conductivity, S/cm
φ	Potential, V

Subscripts

full	Full cell
neg	Contribution from negative electrode
pos	Contribution from positive electrode
N212	Nafion 212
N115	Nafion 115
e	Electrode
S	Solid phase
L	Liquid phase
F	faradaic
half	Half-cell
app	Applied

Superscripts

HF	High-frequency; derived from high frequency impedance
DC	Direct-current; derived from direct current polarization curves
eff	Effective; derived from power dissipation

References

1. G. L. Soloveichik, Flow Batteries: Current Status and Trends. *Chem Rev* **115**(20), 11533 (2015).
2. K. Lin, Q. M. R. Chen Gerhardt, L. Tong, S. B. Kim, L. Eisenach, A. W. Valle, D. Hardee, R. G. Gordon, M. J. Aziz, and M. P. Marshak, Alkaline Quinone Flow Battery. *Science* **349**, 1529 (2015).
3. B. Huskinson, M. P. Marshak, C. Suh, S. Er, M. R. Gerhardt, C. J. Galvin, X. Chen, A. Aspuru-Guzik, R. G. Gordon, and M. J. Aziz, A Metal-Free Organic-Inorganic Aqueous Flow Battery. *Nature*, **505**, 195 (2014).
4. Q. Chen, M. R. Gerhardt, L. Hartle, and M. J. Aziz, A Quinone-Bromide Flow Battery with 1 W/cm^2 Power Density. *Journal of the Electrochemical Society* **163**, A5010 (2015).
5. J. Rugolo, B. Huskinson, and M. J. Aziz, Model of Performance of a Regenerative Hydrogen Chlorine Fuel Cell for Grid-Scale Electrical Energy Storage. *Journal of The Electrochemical Society*, **159**, 133 (2011).
6. D. Aaron, Z. Tang, A. B. Papandrew, and T. A. Zawodzinski, Polarization Curve Analysis of All-Vanadium Redox Flow Batteries. *Journal of Applied Electrochemistry*, **41**, 1175 (2011).
7. R. M. Darling and M. L. Perry, The Influence of Electrode and Channel Configurations on Flow Battery Performance. *Journal of the Electrochemical Society*, **161**, A1381 (2014).
8. J. Newman and C. Tobias, Theoretical Analysis of Current Distribution in Porous Electrodes. *Journal of the Electrochemical Society*, **109**, 1183 (1962).
9. M. Vynnycky, Analysis of a Model for the Operation of a Vanadium Redox Battery. *Energy*, **36**, 2242 (2011).
10. C. N. Sun, F. M. Delnick, D. S. Aaron, A. B. Papandrew, M. M. Mench, and T. A. Zawodzinski, Resolving Losses at the Negative Electrode in All-Vanadium Redox Flow Batteries Using Electrochemical Impedance Spectroscopy. *Journal of the Electrochemical Society*, **161**, A981 (2014).
11. M. Fleischmann , A Palladium-Hydrogen Probe Electrode for Use as a Microreference Electrode. *J. Phys. E: Sci. Intrum.*, **1**, 667 (1968).
12. Z. Liu, J. S. Wainright, W. Huang, and R. F. Savinell, Positioning the Reference Electrode in Proton Exchange Membrane Fuel Cells: Calculations of Primary and Secondary Current Distribution. *Electrochimica Acta*, **49**, 923 (2004).
13. Q. Liu, A. Turhan, T. A. Zawodzinski, and M. M. Mench, In Situ Potential Distribution Measurement in an All-Vanadium Flow Battery. *Chem Commun (Camb)*, **49**, 6292 (2013).
14. A. Lasia, Electrochemical Impedance Spectroscopy and Its Applications. In *Modern Aspects of Electrochemistry*, B. E. Conway J. O. M. Bockris R. E. White, Eds. Springer US: Boston, MA, 2002; pp 143.
15. Z. Tang, R. Svoboda, J. S. Lawton, D. S. Aaron, A. B. Papandrew, and T. A. Zawodzinski, Composition and Conductivity of Membranes Equilibrated with Solutions of Sulfuric Acid and Vanadyl Sulfate. *Journal of The Electrochemical Society*, **160**, F1040 (2013).
16. J. Newman and W. Tiedemann, Porous-Electrode Theory with Battery Applications. *AIChE J.*, **21**, 25 (1975).
17. Q. H. Liu, G. M. Grim, A. B. Papandrew, A. Turhan, T. A. Zawodzinski, and M. M. Mench, High Performance Vanadium Redox Flow Batteries with Optimized Electrode Configuration and Membrane Selection. *Journal of the Electrochemical Society*, **159**, A1246 (2012).
18. H. Zhou, H. Zhang, P. Zhao, and B. Yi, A Comparative Study of Carbon Felt and Activated Carbon Based Electrodes for Sodium Polysulfide/Bromine Redox Flow Battery. *Electrochimica Acta*, **51**, 6304 (2006).